Photon efficient orientation estimation using polarization modulation in single-molecule localization microscopy

Thorsen, Rasmus; Hulleman, Christiaan N.; Rieger, Bernd; Stallinga, Sjoerd

DOI
10.1364/BOE.452159

Publication date
2022

Document Version
Final published version

Published in
Biomedical Optics Express

Research Article | Vol. 13, No. 5 / 1 May 2022 / Biomedical Optics Express 2835
Biomedical Optics EXPRESS

Photon efficient orientation estimation using polarization modulation in single-molecule localization microscopy

RASMUS Ø. THORSEN,[1,2] CHRISTIAAN N. HULLEMAN,[1,2] BERND RIEGER,[1,2,3] AND SJOERD STALLINGA[1,2,4]

[1]Department of Imaging Physics, Delft University of Technology, Delft, The Netherlands
[2]These authors contributed equally
[3]b.rieger@tudelft.nl
[4]s.stallinga@tudelft.nl

Abstract: Combining orientation estimation with localization microscopy opens up the possibility to analyze the underlying orientation of biomolecules on the nanometer scale. Inspired by the recent improvement of the localization precision by shifting excitation patterns (MINFLUX, SIMFLUX), we have adapted the idea towards the modulation of excitation polarization to enhance the orientation precision. For this modality two modes are analyzed: i) normally incident excitation with three polarization steps to retrieve the in-plane angle of emitters and ii) obliquely incident excitation with p-polarization with five different azimuthal angles of incidence to retrieve the full orientation. Firstly, we present a theoretical study of the lower precision limit with a Cramér-Rao bound for these modes. For the oblique incidence mode we find a favorable isotropic orientation precision for all molecular orientations if the polar angle of incidence is equal to $\arccos\sqrt{2/3} \approx 35$ degrees. Secondly, a simulation study is performed to assess the performance for low signal-to-background ratios and how inaccurate illumination polarization angles affect the outcome. We show that a precision, at the Cramér-Rao bound (CRB) limit, of just 2.4 and 1.6 degrees in the azimuthal and polar angles can be achieved with only 1000 detected signal photons and 10 background photons per pixel (about twice better than reported earlier). Lastly, the alignment and calibration of an optical microscope with polarization control is described in detail. With this microscope a proof-of-principle experiment is carried out, demonstrating an experimental in-plane precision close to the CRB limit for signal photon counts ranging from 400 to 10,000.

1. Introduction

Single-Molecule Localization Microscopy (SMLM) is an established super-resolution microscopy technique, taking image resolution from the ~ 200 nm diffraction limit down to the 20 nm regime with many imaging modalities such as (f)PALM [1,2], STORM [3] and PAINT [4]. SMLM uses emitters that can switch between off- and on-states such that only a sparse subset of all emitters is active in each image frame of a time series. This temporal modulation allows the active emitters to be localized with a precision an order of magnitude below the diffraction limit. Localizations in different time frames accumulate to a list of emitter positions rather than pixel-based images, which means that the image is constituted by a list of single molecule data. New SMLM image modalities can be created by extending this list beyond the x and y coordinates of the molecules [5]. In this paper we focus on the extension with molecular orientation parameters [6]. Typically the emitters are assumed to rotate freely during the emission states. However, cases exist where the emitters have a fixed pose and therefore experience little rotational diffusion, e.g., when rigidly bound to a target [7–9] or immobilized at a surface [10,11]. The emitter orientation

#452159 https://doi.org/10.1364/BOE.452159
Journal © 2022 Received 18 Jan 2022; revised 31 Mar 2022; accepted 3 Apr 2022; published 21 Apr 2022

Biomedical Optics EXPRESS

provides insight into the linking properties and must otherwise be taken into account explicitly as it affects the localization precision [12,13].

The Point Spread Function (PSF) of conventional widefield fluorescence microscopy is poorly suited for orientation estimation because of inherent symmetries such as the symmetry between positions above and below the nominal focus plane. Therefore the imaging system must be altered for extracting this additional information. A first effort was based on defocused imaging for increasing the variance of the PSF shape with molecular orientation [8]. A major drawback is that the defocus spreads the limited number of signal photons across more pixels, which degrades the localization precision. Long exposures are therefore needed to overcome this photon dilution, making these methods less ideal for localization microscopy. An alternative way to increase the orientation information has been with proposed engineered PSFs [14–16], which can be realized experimentally by adding a phase-shaping element in the optical pathway before the camera. These PSFs vary in shape and performance, yet they commonly increase the PSF size and thereby hinder optimum detection at low signal-to-background ratios (SBRs).

The polarization of the fluorescence excitation and emission is directly coupled to the molecular orientation and therefore offers a direct way to probe orientation. The use of the polarization of the emitted light usually involves placing a polarizing beam splitter in the detection light path to separately collect different polarization components on the camera. The intensity in these sub-images is used as a parametric indicator of molecular orientation [17–21], which can also be combined with PSF engineering approaches [22–25]. Application of excitation polarization modulation has been studied in simulations [26,27], with notable demonstrations on single fluorophores [28] and biomolecules [29]. It has, however, rarely been applied in the context of SMLM until Backer, Lee, and Moerner used a sequence of images generated with a normally incident illumination beam with linear polarization that toggles between three different directions [30]. In this technique, three sequential images are used to estimate the in-plane orientation of single molecules. The key advantage of using excitation polarization over emission polarization fitting is that the signal photons are not spread out over a larger area on the camera than the area of a diffraction-limited spot. This implies that extracting orientational information can be expected to be more efficient for excitation polarization schemes at low photon counts, i.e. if the SBR is unfavorable.

In this paper we build on the polarization modulation scheme of Ref. [30] by a Cramér-Rao Bound (CRB) analysis of the best possible achievable precision, and by a simulation study of the impact of signal photon count, SBR, and polarization purity on precision. The analysis uses a comprehensive Maximum Likelihood Estimation (MLE) method for simultaneous estimation of position and orientation, improving the routine used by Backer, Lee, and Moerner that neglects spot shape [31]. In a next step, we describe a method to overcome a major drawback of the method presented in Ref. [30], namely the inability to estimate the out-of-plane, polar angle of the emission dipole of the molecules. This is achieved by changing the illumination from normal incidence to oblique incidence. In the case of oblique incidence the illumination polarization can have a sizeable component along the optical axis, which is used to extract the full orientation (both polar and azimuthal angle). Our re-examination of polarization modulation was inspired by the recent development of modulation-enhanced localization. A series of such estimators have emerged initiated by the work on MINFLUX [32], later followed by SIMFLUX [33] and related proposals [34,35]. In these concepts a spatially shifting non-uniform illumination pattern is used to improve localization precision, e.g. a standing wave pattern leads to a twofold improvement [33].

The outline of this paper is as follows. We first expand the imaging model by incorporating the excitation efficiency in the signal strength (photon count) by the conventional square of the cosine of the angle between polarization and dipole orientation. We describe a general framework that incorporates both normal and oblique incidence, even for large angles of incidence that

Biomedical Optics EXPRESS

may give rise to evanescent wave illumination in Total Internal Reflection Fluorescence (TIRF) imaging [36]. Next, we set up the MLE framework that underlies the CRB analysis. We use this framework for a general theoretical analysis and in our simulation study, in conjunction with a proper vectorial PSF model. Thereafter, we describe the optical microscope setup and necessary calibration steps to achieve the desired polarization states. This setup is used for a proof-of-principle experiment for the MLE framework with vectorial PSF model, which enables a demonstration of experimental precision of the in-plane orientation of immobilized fluorophores at the level of the CRB. The paper is concluded with a discussion of the results and an outlook on next steps.

2. Theory

2.1. Fluorescence excitation model

Figure 1 shows our concept of polarization modulation and spot shape detection. We start by assuming that a single common absorption and emission dipole axis completely describes the emitter's orientation [37]. This orientation is parameterized by the space angle $\Omega = (\phi, \theta)$, a shorthand notation for the combination of azimuthal angle $0 \leq \phi \leq 2\pi$ and polar angle $0 \leq \theta \leq \pi$, or equivalently by its dipole moment along the unit vector $\hat{\mathbf{d}} = (\sin\theta\cos\phi, \sin\theta\sin\phi, \cos\theta)$ (Fig. 1(a)). This assumption is usually true as most fluorescent molecules are well-approximated as electric dipoles [38].

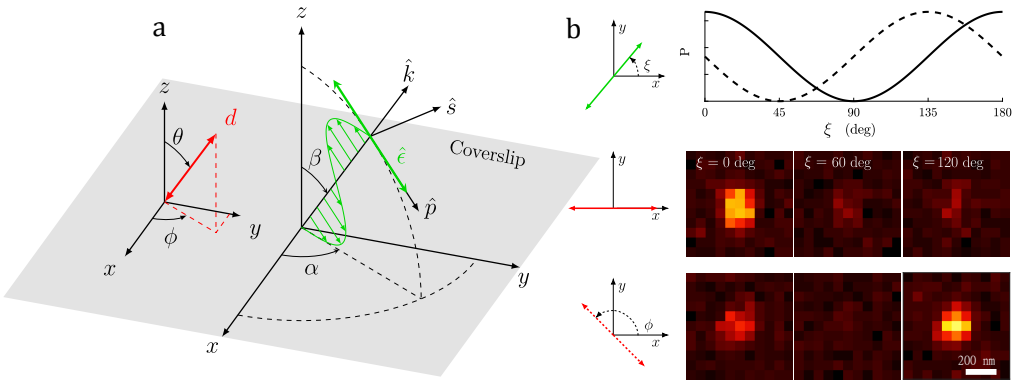

Fig. 1. Polarization modulation and spot shape detection. (a) A constrained dipole is characterized by its azimuthal angle ϕ and a polar angle θ, or equivalently its dipole moment orientation $\hat{\mathbf{d}}$. The dipole is excited by a plane wave with a direction along the wavevector $\hat{\mathbf{k}}$ with incidence angles α and β, and a polarization state $\hat{\boldsymbol{\epsilon}}$ that lies in the plane perpendicular to the wave vector with components $\hat{\mathbf{p}}$ and $\hat{\mathbf{s}}$. (b) Example of combined estimation for normal ($\alpha = \beta = 0$) excitation with polarization rotation angle ξ. A total of three images are recorded with shifted polarization states at $\xi = [0°, 60°, 120°]$ for two dipole emitters with in-plane angles $\phi = 0°$ and $\phi = 135°$. Combining the shape information of the three frames with the photon count in relation to the polarization shift improves the precision.

The fluorescence excitation efficiency depends on the orientation of this transition moment with respect to the electric field vector of the excitation light:

$$\mathbf{E} = E\hat{\boldsymbol{\epsilon}} \exp(-i\omega t) \tag{1}$$

with E the magnitude, ω the radial frequency, and t time. The complex vector $\hat{\boldsymbol{\epsilon}}$ fully describes the polarization state and this vector satisfies $|\hat{\boldsymbol{\epsilon}}| = 1$. For a propagating plane wave, the polarization ellipse described by $\hat{\boldsymbol{\epsilon}}$ is perpendicular to the unit vector along the direction of propagation given

Biomedical Optics EXPRESS

by the wavevector $\hat{\mathbf{k}} = (\sin\beta\cos\alpha, \sin\beta\sin\alpha, \cos\beta)$, where $\alpha\,[0, 2\pi)$ and $\beta\,[0, \pi/2]$ defines the azimuthal and polar angle of incidence. In the plane perpendicular to this unit vector, the polarization ellipse can be parameterized by an amplitude ratio $\tan\nu$ and a phase delay 2δ leading to:

$$\hat{\boldsymbol{\epsilon}} = \cos\nu\, e^{-i\delta}\hat{\mathbf{p}} + \sin\nu\, e^{i\delta}\hat{\mathbf{s}}, \tag{2}$$

with the components $\hat{\mathbf{p}} = (\cos\beta\cos\alpha, \cos\beta\sin\alpha, -\sin\beta)$ and $\hat{\mathbf{s}} = (-\sin\alpha, \cos\alpha, 0)$. In Fig. 2(a) the ellipticity angle $\tau\,(-\pi/4, \pi/4]$ and long axis orientation of the polarization ellipse ξ are related to the parameters $\nu\,[0, \pi/2]$ and $\delta\,[0, 2\pi)$ via the Stokes-vector components:

$$S_1 = \cos(2\nu) = \cos(2\tau)\cos(2\xi), \tag{3a}$$

$$S_2 = \sin(2\nu)\cos(2\delta) = \cos(2\tau)\sin(2\xi), \tag{3b}$$

$$S_3 = \sin(2\nu)\sin(2\delta) = \sin(2\tau), \tag{3c}$$

that satisfy $S_1^2 + S_2^2 + S_3^2 = 1$, i.e., Poincaré-sphere coordinates as shown in Fig. 2(b) [39]. The ellipticity angle $|\tau| \le \pi/4$ has limiting cases $\tau = 0$ and $|\tau| = \pi/4$ for linearly and circularly polarized excitation, respectively.

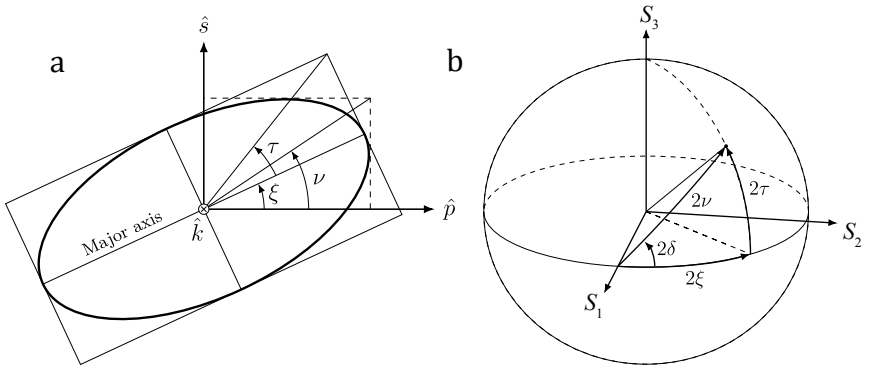

Fig. 2. Polarization angles. (a) Polarization ellipse characterized by its major axis angle ξ and ellipticity angle τ or an amplitude angle ν together with the phase delay δ. (b) Poincaré representation of the state of polarization.

If the molecule is effectively stationary during the measurement time, according to the dipole approximation, the measured intensity is proportional to the square of the projection of the transition dipole moment onto the polarization state's direction. Then a fluorophore contributes to the fluorescence signal over a sequence of $m = 1, 2, \ldots, M$ camera frames with changing polarization excitation state $\hat{\boldsymbol{\epsilon}}_m$:

$$\begin{aligned} Q_m(\Omega) &= \left|\hat{\mathbf{d}}\cdot\hat{\boldsymbol{\epsilon}}_m\right|^2 \\ &= \frac{1}{2}\left[\left|\hat{\mathbf{d}}\cdot\hat{\mathbf{p}}\right|^2 + \left|\hat{\mathbf{d}}\cdot\hat{\mathbf{s}}\right|^2\right] + \frac{1}{2}\left[\left|\hat{\mathbf{d}}\cdot\hat{\mathbf{p}}\right|^2 - \left|\hat{\mathbf{d}}\cdot\hat{\mathbf{s}}\right|^2\right] S_1 \\ &+ \mathrm{Re}\left\{\left(\hat{\mathbf{d}}\cdot\hat{\mathbf{p}}\right)\left(\hat{\mathbf{d}}\cdot\hat{\mathbf{s}}\right)^*\right\} S_2 + \mathrm{Im}\left\{\left(\hat{\mathbf{d}}\cdot\hat{\mathbf{p}}\right)\left(\hat{\mathbf{d}}\cdot\hat{\mathbf{s}}\right)^*\right\} S_3 \end{aligned} \tag{4}$$

The polarization states $\hat{\boldsymbol{\epsilon}}_m$ are typically chosen equally spaced over the minimal amount of states M required to uniquely define a solution. We define the modulation function as:

$$P_m(\Omega) = \frac{Q_m(\Omega)}{Q_{\mathrm{norm}}} \tag{5}$$

Biomedical Optics EXPRESS

where Q_{norm} is a normalization condition that depends on the excitation mode such that:

$$\sum_{m=1}^{M} P_m(\Omega) = 1. \tag{6}$$

This modulation function $P_m(\Omega)$ serves as the expectation function in the estimation process and may often be reduced to a relatively simple expression depending on the excitation mode.

2.2. Dipole imaging model

The expected photon count (μ_{nm}) at pixel $n = 1, \ldots, N_{\text{pix}}$ is modulated with the function $P_m(\Omega)$ (Eq. (5)) over a sequence of $m = 1, \ldots, M$ frames with different excitation polarization states. This expected count depends on the emitter position $\mathbf{r}_0 = (x_0, y_0)$, the total signal photon count N and background photons per pixel b, and the dipole orientation Ω, given a total of 6 parameters to be estimated. The expected photon count is given by:

$$\mu_{nm} = NP_m(\Omega)H_n(\mathbf{r}_0, \Omega) + \frac{b}{a^2 M} \tag{7}$$

where a is the pixel size and $H_n(\mathbf{r}_0, \Omega)$ is the expected fluorescence intensity distribution of pixel n for a fluorophore at position $\mathbf{r}_0$ and with orientation Ω, normalized such that:

$$\sum_{n} H_n(\mathbf{r}_0, \Omega) = 1. \tag{8}$$

The normalized fluorescence intensity is computed using the vectorial PSF model described elsewhere [40,41]. For the sake of completeness, the details are presented in the Supplement 1 (section 1). We use standard Maximum Likelihood Estimation (MLE) methods based on the Poissonian noise distribution to find the 6 parameters $(x_0, y_0, N, b, \theta, \phi)$ that best fit the observed single molecule images [42,43].

3. Evaluation of Fisher-information and Cramér-Rao bounds

The expected precision for estimating the different parameters can be assessed by developing an approximation to the Fisher-matrix and the Cramér-Rao bound (CRB). Here we focus on the modulated parameters Ω as the unmodulated ones behave as in standard SMLM, which have been investigated extensively previously [40,44]. The starting point to retrieve the Fisher-information matrix is the log-likelihood function, where its derivatives with respect to the parameters give rise to the Fisher-information elements [43]. These can be expressed in closed-form if we ignore the finite pixel size, neglect the region of interest's (ROI) finite support, and assume zero background. Following the approach in [33] with the imaging model given by Eq. (7), the Fisher-matrix elements involving the modulated parameters become:

$$F_{\Omega\Omega} = N \sum_{n=1}^{N_{\text{pix}}} \frac{1}{H_n(\mathbf{r}_0, \Omega)} \left(\frac{\partial H_n(\mathbf{r}_0, \Omega)}{\partial \Omega} \right)^2 + N \sum_{m=1}^{M} \frac{1}{P_m(\Omega)} \left(\frac{\partial P_m(\Omega)}{\partial \Omega} \right)^2 \tag{9}$$

where the first term arises from orientation-induced information in the shape of the PSF, the same as for conventional SMLM, and where the second term originates from the polarization modulation. This second term implies that modulation makes these diagonal Fisher-matrix elements larger and hence the associated CRB smaller due to the inversion relation $\text{CRB}_\Omega = [F_{\Omega\Omega}]^{-1}$, provided the off-diagonal mixing between the orientational parameters Ω and the other parameters can be neglected. In any case, the average CRB, equal to the average of the diagonal elements of the inverse of the Fisher matrix, is always smaller than the inverse of the average of the diagonal

Biomedical Optics EXPRESS

elements of the Fisher matrix (this is true for any symmetric matrix). It then follows that the modulation terms necessarily decrease the average of the CRBs of all estimated parameters.

A simplified approach to assess the impact of modulation is to evaluate Eq. (9) under the assumption that the contribution to the Fisher-information from modulation is much larger than the contribution from the PSF shape variations, i.e., the orientation dependency of the PSF is neglected (e.g., for a 2D Gaussian model). This assumption is, however, not used for the actual numerical parameter estimation in simulation later.

3.1. Normal incidence

For normally incident light ($\alpha = \beta = 0$) the polarization vector is restricted to the xy imaging plane ($\epsilon_z = 0$). The non-zero components of the polarization vector are $\epsilon_x = \cos\xi\cos\tau - i\sin\xi\sin\tau$ and $\epsilon_y = \sin\xi\cos\tau + i\cos\xi\sin\tau$, with ξ the in-plane orientation of the polarization ellipse and with τ the ellipticity angle (Fig. 2). The polarization modulation is implemented by rotating the long axis of the polarization ellipse with equidistant angles $\xi_m = \pi(m-1)/M + \xi_0$, $s = 1, 2, \ldots, M$. The angles are taken relative to the x axis with offset ξ_0, and the number of polarization steps must be $M \geq 3$ to ensure the uniqueness of the solution. Note that the scan range of the equidistant phases is over the π phase range, which is enough to span the polarization plane due to the head-tail symmetry of the dipole axis. Now Eq. (4) gives:

$$Q_m(\theta, \phi) = \frac{\sin^2\theta}{2}\left[1 + \cos(2\tau)\cos\left(2\phi - 2\xi_m\right)\right] \tag{10}$$

so that $Q_{\text{norm}} = M\sin^2\theta/2$ which makes:

$$P_m(\phi) = \frac{1}{M}\left[1 + \cos(2\tau)\cos\left(2\phi - 2\xi_m\right)\right] \tag{11}$$

a function of the azimuthal angle ϕ only. It is seen that the modulation contrast is degraded by the ellipticity factor $\cos(2\tau)$, where $\tau = 0$ results in the often-used cosine squared scaling factor $\cos^2(\phi - \xi_m)$, whereas in the case $|\tau| = \pi/4$ no modulation occurs. This modulation factor results in a CRB with a slight dependence on the dipole azimuthal angle ϕ, making the precision somewhat anisotropic. Figure 3(a) shows this dependence indicating a strong response on τ close to $\tau \approx 0$ for dipole orientations aligned perpendicular to one of the applied polarizations. These sharp peaks are mitigated in practice due to non-zero background, as indicated with the gray line in Fig. 3(a).

The modulation only approximation to the Fisher-information can be deduced by substituting Eq. (11) in the second term of Eq. (9) and computing the sum over the different excitation polarizations:

$$F_{\phi\phi} = \frac{4N}{M}\sum_{m=1}^{M}\frac{\cos^2(2\tau)\sin^2(2\phi - 2\xi_m)}{1 + \cos(2\tau)\cos(2\phi - 2\xi_m)}. \tag{12}$$

The average Fisher-information over all the molecule orientations follows as:

$$\tilde{F}_{\phi\phi} = \frac{1}{2\pi}\int_0^{2\pi} \mathrm{d}\phi\, F_{\phi\phi} = 4N(1 - 2\cos\tau\,|\sin\tau|) \tag{13}$$

where the integral over ϕ can be evaluated using contour integration in the complex plane (substitute $z = \tan\phi$) or by using a computer algebra system. This result in the average precision bound:

$$\tilde{\sigma}_\phi \geq \frac{1}{2\sqrt{N}}\frac{1}{\sqrt{1 - 2\cos\tau|\sin\tau|}} \tag{14}$$

independent of the angle offset ξ_0 and referred to here as the modulation only precision. The scaling with $1/\left(2\sqrt{N}\right)$ for linear polarization is a factor $\sqrt{2}$ better than the scaling found for polarimetric detection schemes [19,45].

Biomedical Optics EXPRESS

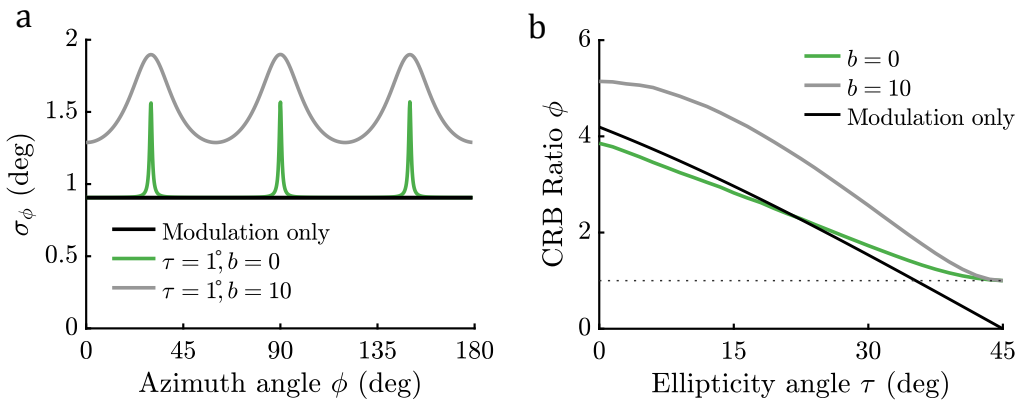

Fig. 3. CRB performance for normally incident polarization. (a) The azimuth angle precision σ_ϕ as a function of the dipole azimuth angle ϕ with polar angle $\theta = \pi/2$ using $M = 3$ polarization steps $\xi_m = [0°, 60°, 120°]$. The precision is computed using Eq. (14) with different ellipticity angles τ and numerically with background photons per pixel b. (b) The CRB ratio is computed as the average CRB from the polarization modulation relative to the standard (non-modulated) PSF and is shown as a function of the ellipticity angle. The modulation only precision curve is calculated from Eq. (14) and is relative to the standard (non-modulated) PSF. The black dashed line indicates no improvement, i.e., a CRB ratio of 1. All plots are computed with a photon count of $N = 1000$ and the dipole simulations assume matched imaging conditions $n = 1.518$.

This modulation only CRB is plotted relative to the CRB of the standard (non-modulated, $M = 1$) PSF in Fig. 3(b) as a function of the ellipticity angle τ. The goal of this comparison is to elucidate the relative impact of modulation on precision, not to benchmark performance to state-of-the-art methods. The CRB of the PSF shape is computed numerically from simulated dipole images. The comparison supports the assumption that the modulation term dominates the Fisher-information, at least for the regime τ<30°. It is likewise seen that the effects of finite support of the fitting Region Of Interest (ROI) and finite pixel size are negligible. The CRB ratio indicates that the precision improves up to four-fold ($\tau = 0$) by the polarization modulation. The CRB ratio in the presence of background ($b = 10$ counts/pixel) is also numerically computed, where the CRB ratio is found to increase to around five. This indicates that the polarization modulation precision scales better with background than the precision based on PSF shape alone. The average precision for $N = 1000$ with zero background ($b = 0$) is $\sigma_\phi = 0.99°$ ($\sigma_\phi = 3.8°$ for $\tau = \pi/4$), whereas for $b = 10$ it is $\sigma_\phi = 1.5°$ ($\sigma_\phi = 7.7°$ for $\tau = \pi/4$).

3.1.1. Comparison to other methods

Polarization modulation performs favourably compared to other in-plane orientation estimation techniques like polarization split detection. Comparing the two under similar conditions, a CRB of $\sigma_\phi = 2.4°$ and $\sigma_{xy} = 6.8$ nm is found with our polarization modulation method compared to $\sigma_\phi = 4°$ and $\sigma_{xy} = 10$ nm when using a polarized PSF ($N = 380$, $b = 2$, $\phi = 135°$, NA= 1.4, $\lambda = 610$ nm and pixel size = 58.5 nm) [46]. This illustrates the azimuthal precision improvement by a factor of $\sqrt{2}$ by using polarization modulation over polarimetric detection schemes. Splitting s and p polarized light introduces an ambiguity for $\phi = \pm 45°$, this can be avoided by splitting the polarization into four as investigated in [19] and recently implemented in 4polar-STORM [21]. Comparing to 4polar-STORM (Monte-Carlo analysis not CRB) [21], we find a lateral precision of $\sigma_{xy} = 3.4$ nm with polarization modulation compared to $\sigma_{xy} \sim 18$ nm for 4polar-STORM ($N = 1500$, $b = 40$, $\theta = 90°$, in-plane wobble angle $\delta = 20°$,

Biomedical Optics EXPRESS

NA= 1.2, λ = 520 nm, n_{meduim} = 1.33, and pixel size = 130 nm), and an azimuthal precision of $\sigma_\phi = 1.2°$ with polarization modulation compared to $\sigma_\phi \sim 4°$ for 4polar-STORM (same parameters except $\theta = 60°$ and 3D wobble angle $\delta_{3D} = 20°$). Furthermore, our implementation of polarization modulation is better than the experimental results of the original polarization modulation method presented in Ref. [30]. There, an experimentally obtained precision of $\sigma_\phi = 233.9/\sqrt{N = 1000} \approx 7.4°$ for molecules in PMMA (Polymethyl methacrylate) with 50 background counts per pixel per frame is reported. For the same photon counts, we assess the CRB to be around 3.0°. This difference could be due to experimental inaccuracies, not taking the PSF shape into account, or the non-MLE based estimation method [31].

3.2. Oblique excitation

Favorable precision levels can be achieved for both the azimuthal and polar angle of the molecule if we generalize the previous scheme to obliquely incident light. This approach to polarization modulation uses the polarization component along the optical axis to probe the polar angle. For the sake of simplicity, we ignore ellipticity now and consider only linearly polarized light along the $\hat{\mathbf{p}}$ direction, i.e., $\xi = \tau = 0$. Modulation of polarization is achieved by rotating the direction of incidence around the z-axis, i.e., we take the tilt angle β constant and use azimuthal angles of incidence with equidistant steps $\alpha_m = 2\pi(m-1)/M$. We now find that:

$$Q_m(\phi,\theta) = (\sin\theta\cos\beta\cos(\phi-\alpha_m) - \cos\theta\sin\beta)^2 \tag{15}$$

giving rise to a normalization factor:

$$Q_{\text{norm}} = \frac{M}{2} f(\theta) \tag{16}$$

with angular dependence:

$$f(\theta) = \cos^2\beta - (3\cos^2\beta - 2)\cos^2\theta. \tag{17}$$

The relevant angular derivatives of the expectation function $P_m(\theta,\phi)$ are:

$$\frac{\partial P_m(\theta,\phi)}{\partial\phi} = -\frac{4}{Mf(\theta)}\sqrt{Q_m}\sin\theta\cos\beta\sin(\phi-\alpha_m) \tag{18a}$$

$$\frac{\partial P_m(\theta,\phi)}{\partial\theta} = \frac{4}{Mf(\theta)}\left[\sqrt{Q_m}(\cos\theta\cos\beta\cos(\phi-\alpha_m) + \sin\theta\sin\beta) - \frac{Q_m}{f(\theta)}\left(3\cos^2\beta - 2\right)\cos\theta\sin\theta\right] \tag{18b}$$

where $Q_m = Q_m(\phi,\theta)$ (Eq. (15)). These derivatives leads to the modulation-only diagonal Fisher-matrix elements:

$$F_{\phi\phi} = \frac{8N\sin^2\theta\cos^2\beta}{Mf(\theta)}\sum_{m=1}^{M}\sin^2(\phi-\alpha_m) = \frac{4N\sin^2\theta\cos^2\beta}{f(\theta)} \tag{19a}$$

$$F_{\theta\theta} = \frac{8N\cos^2\beta\sin^2\beta}{f^3(\theta)}\left[f(\theta) + \frac{c_1}{M}\sum_{m=1}^{M}\cos(2\phi-2\alpha_m) + \frac{c_2}{M}\sum_{m=1}^{M}\cos(\phi-\alpha_m)\right] = \frac{8N\cos^2\beta\sin^2\beta}{f^2(\theta)} \tag{19b}$$

Biomedical Optics EXPRESS

where $c_1 = 2\cos^2\theta\sin^2\beta$ and $c_2 = \sin(2\theta)\sin(2\beta)$. The off-diagonal Fisher-matrix element:

$$F_{\phi\theta} = N\sum_{m=1}^{M}\frac{1}{P_m}\frac{\partial P_m}{\partial\theta}\frac{\partial P_m}{\partial\phi} \tag{20}$$

contains terms that are either proportional to:

$$\sum_{m=1}^{M}\sin\left(\phi-\alpha_m\right) = 0 \tag{21}$$

or to:

$$\sum_{m=1}^{M}\sin\left(\phi-\alpha_m\right)\cos\left(\phi-\alpha_m\right) = 0 \tag{22}$$

and hence evaluates to zero. This implies that the precision bounds are:

$$\sigma_\phi \geq \frac{\sqrt{f(\theta)}}{2\sin\theta\cos\beta\sqrt{N}} \tag{23a}$$

$$\sigma_\theta \geq \frac{\sqrt{2}f(\theta)}{4\sin\beta\cos\beta\sqrt{N}}. \tag{23b}$$

Figure 4 shows these precision bounds as calculated for the azimuthal, polar, and combined (solid angle) precision $\sigma_\Omega = \sin\theta\sigma_\theta\sigma_\phi$ as a function of the angle of incidence β and the polar dipole angle θ. It appears that for $\beta <$ arccos$(\sqrt{2/3}) \approx 35°$ the precision improves with decreasing polar angle θ, whereas for $\beta >$ arccos$(\sqrt{2/3})$ the precision improves with increasing polar angle θ. In general there is no a priori information on the distribution of polar dipole angles, implying that the choice $\beta =$ arccos$(\sqrt{2/3})$ is ideal as it generates an isotropic precision. Another favourable effect of choosing this angle of incidence is that it makes the photon detection efficiency, proportional to Q_{norm}, independent of molecular orientation. This angle of incidence leads to the simplified modulation only precision bounds for oblique illumination:

$$\sigma_\phi \geq \frac{1}{2\sin\theta\sqrt{N}} \tag{24a}$$

$$\sigma_\theta \geq \frac{1}{2\sqrt{N}} \tag{24b}$$

where we used $\cos\beta = \sqrt{2/3}$ and $\sin\beta = \sqrt{1/3}$ to simplify the results. The combined precision in terms of solid angle for this angle of incidence is now $\sigma_\Omega = 1/(4N)$, uniform over the unit sphere representing all dipole orientations. The bounds in Eq. (24) (with $N = 1$) match the quantum limits for orientation estimation (in the high NA limit where the chance of capturing a photon from a z oriented molecule is equal to that of an in-plane molecule) [47]. There will also be variations in photon detection efficiency with polar angle, that may be quantified by the ratio $f(\theta = 0)/f(\theta = \pi/2) = 2\tan^2\beta$.

The modulation only precision, shown in Fig. 5 is compared to the numerical simulations with varying ellipticity angle and background levels. The CRB precision over the entire sphere of dipole orientations is displayed in Fig. 5(a,d) with an ellipticity angle of 1°, where the peaks of deteriorated precision are now relative to the five polarization planes. Figure 5(b,e) shows the azimuth and polar angle precision dependency along the molecules polar angle with constant $\phi = 0$ for different polarization ellipticity and background photon counts. The obtained CRB is plotted relative to the CRB of the standard (non-modulated, $M = 1$) PSF in Fig. 5(c,f) as a

Biomedical Optics EXPRESS

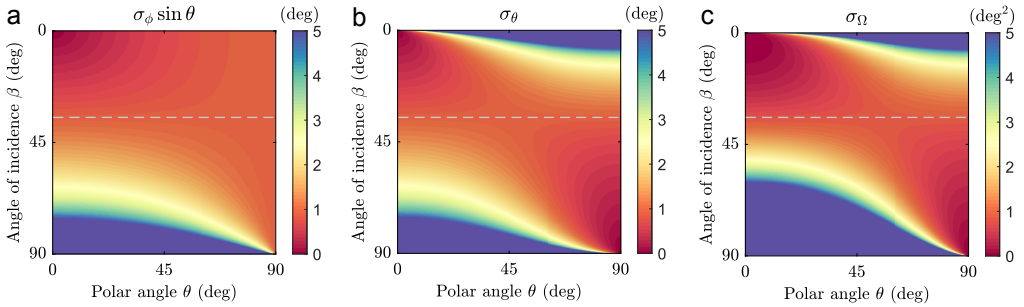

Fig. 4. Impact of the angle of incidence on the CRB. (a) The precision of the dipole azimuth angle σ_ϕ scaled by a factor $\sin\theta$, (b) polar angle precision σ_θ, and (c) solid angle orientation precision σ_Ω as a function of the dipole polar angle θ and angle of incidence β using Eq. (23). The gray dashed line is used to guide the eye for $\beta = \arccos(\sqrt{2/3}) \approx 35°$. All plots are computed with $N = 1000$.

function of the polarization ellipticity angle τ. The CRB ratio indicates that the modulation improves the orientation precision by a factor of 7.6 and 4.7 for the azimuth and polar angle in the case of zero background and scales up to a factor of 14.4 and 7.8 in the case of 10 background photons per pixel.

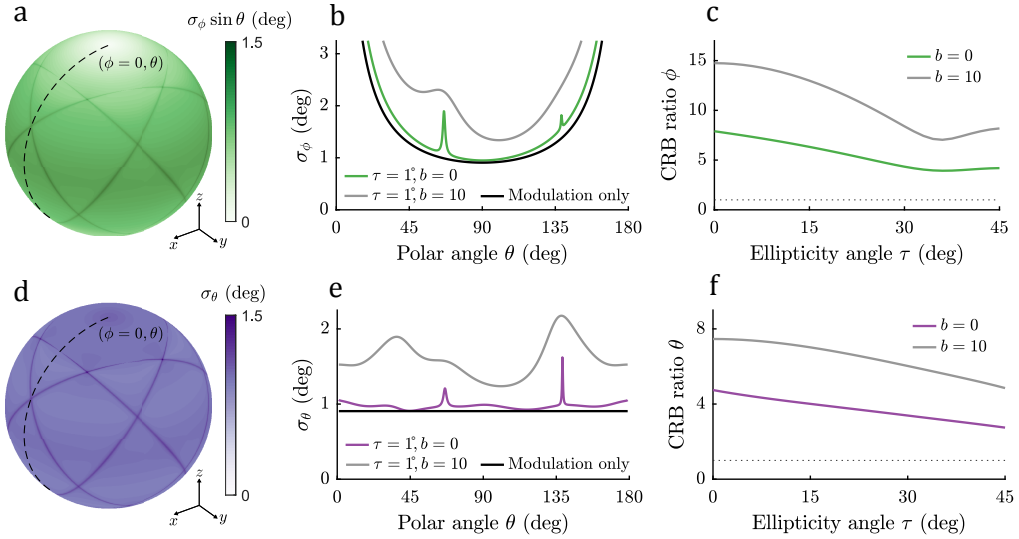

Fig. 5. CRB performance for oblique polarization. (a) The azimuth angle precision σ_ϕ scaled by $\sin\theta$ over the sphere of orientations for five oblique polarization steps at $\beta = \arccos(\sqrt{2/3})$ and ellipticity $\tau = 1°$. (b) The azimuth angle precision as a function of the dipole angle (θ) along the black dashed line in (a) ($\phi = 0$). The theoretical precision for modulation only is calculated from Eq. (24) and computed numerically with $\tau = 1°$ and different background counts per pixel b otherwise. (c) The azimuth CRB ratio, which is the CRB from the polarization modulation relative to the CRB of the standard (non-modulated, $M = 1$) PSF as a function of the ellipticity angle. The black dashed line indicates no improvement, i.e., a CRB ratio of 1. (d, e, f) Same as above with the polar angle precision. All plots are computed with $N = 1000$ photons and dipole simulations assume matched imaging conditions $n = 1.518$.

Biomedical Optics EXPRESS

3.2.1. Comparison to other methods

Polarization modulation performs well compared to many polarization splitting and PSF engineering methods. The azimuthal and polar precision levels are better than for example the recent Vortex PSF based method [16], though the Vortex PSF is also able to estimate the degree of rotational diffusion and axial position. With polarization modulation we find $\sigma_\phi = 1.7°$, $\sigma_\theta = 1.1°$ and $\sigma_{xy} = 3.6$ nm, compared to the Vortex PSF $\sigma_\phi = 5.5°$, $\sigma_\theta = 3.1°$ and $\sigma_{xy} = 5.6$ nm ($N = 4000$, $b = 10$, NA= 1.45, $\lambda = 597.5$ nm, $n_{\text{meduim}} = 1.333$ and pixel size = 65 nm) [16]. For this CRB evaluation the values of ϕ and θ are averaged over 10,000 values distributed uniformly on a sphere, for the Vortex PSF the dipole orientations are not completely fixed, $g_2 = 0.75$ however these precision values change little between $g_2 = 1$ and $g_2 = 0.75$ as shown in Supplement 1 in [16]. Combining polarization splitting with the Vortex PSF improves the azimuthal precision and estimation of non rationally symmetric rotational diffusion [16,48]. With polarization modulation we find $\sigma_\phi = 3.6°$, $\sigma_\theta = 2.3°$ and $\sigma_{xy} = 7.1$ nm compared to a polarized Vortex PSF $\sigma_\phi = 7.7°$, $\sigma_\theta = 4.5°$ and $\sigma_{xy} = 12.5$ nm ($N = 510$, $b = 2.3$, averaged over 10,000 values of ϕ and θ distributed uniformly on a sphere, NA= 1.4, $\lambda = 593$ nm, $n_{\text{meduim}} = 1.334$, and pixel size = 58.5 nm) [48]. Compared to CHIDO, a polarization splitting method with an additional stress-engineered optic, we find a precision of $\sigma_\phi = 0.5°$, $\sigma_\theta = 0.4°$ and $\sigma_{xy} = 1.1$ nm compared to $\sigma_\phi = 1.1°$, $\sigma_\theta = 1.6°$ and $\sigma_{xy} = 2.7$ nm for CHIDO ($N = 10,000$, $b = 250$, $\theta = 90°$, NA= 1.45, $\lambda = 520$ nm, and pixel size = 67 nm) [24]. Compared to splitting radial and azimuthal polarization (raPol) we find a precision of $\sigma_\phi = 1.1°$, $\sigma_\theta = 0.7°$ and $\sigma_{xy} = 2.1$ nm compared to raPol $\sigma_\phi = 1.4°$, $\sigma_\theta = 1.7°$ and $\sigma_{xy} = 2.2$ nm ($N = 5000$, $b = 30$, averaged over 10,000 values of ϕ and θ distributed uniformly on a sphere, NA= 1.5, $\lambda = 570$ nm, $n_{\text{meduim}} = 1.334$, and pixel size = 66.86 nm) [25].

4. Numerical investigation of estimator performance

We have tested the performance of the combined position and orientation estimator through simulations. We have focused on the impact of the SBR and tolerances for the required set of excitation polarization states at the sample. The latter provides a guideline on how well the microscope must be calibrated.

4.1. Simulation setup

The numerical studies were performed with ground truth dipole images calculated with the vectorial imaging theory (see Supplement 1 section 1) as input to the developed MLE. We used an image plane grid corresponding to a region of interest (ROI) of 11×11 pixels. The optical settings were taken to match our imaging system (section 5.1) with a numerical aperture (NA) of 1.49 and a pixel size of 65 nm in the object space. We assume imaging conditions with refractive indices of 1.33, 1.523, and 1.518 for the imaging medium, cover slip, and immersion medium. Unless stated otherwise, we take 1000 detected photon counts on the camera and 10 background counts per pixel. We neglect readout noise but added Poisson noise to each image with the PSF as the Poisson rate.

The angle of incidence is either $\beta = 0$ (normal incidence) with $M = 3$ or $\beta = \arccos(\sqrt{2/3})$ (oblique incidence) with $M = 5$, where M is the number of different excitation polarizations as outlined in the theory section. Five azimuthal steps were chosen in the case of oblique incidence in order to guarantee the stability of the optimization, even though the theoretical CRB was independent of M. In particular, we found that the sensitivity to the initial values of the parameters in the MLE optimization was unfavorable for three polarization steps, thereby compromising robustness. This behavior is not unreasonable, as now an additional parameter (the polar angle) must be estimated.

Biomedical Optics EXPRESS

The statistical errors were evaluated from 10,000 random instances with dipole positions taken from a uniform distribution over 1 pixel and dipole orientations uniformly distributed over the unit sphere, i.e., $\phi = \pi u$ and $\theta = \arccos(1 - 2u)$ where u is a uniform random number from the distribution $U[0, 1]$.

4.2. Signal-to-background ratio (SBR)

First we quantify the range of photon counts over which the parameters are expected to be estimated reliably. Figure 6 shows the performance as a function of the signal-to-background ratio (SBR = N/b) in the dipole images. For an SBR = 1000/10, the normal incidence polarization mode (averaged over in-plane molecular orientations) gives a localization precision σ_{xy} = 3.6 nm, and an azimuth precision $\sigma_\phi = 1.5°$. The signal count and background photon count precision are σ_N = 42 photons and σ_b = 0.34 photon per pixel (Fig. 6(a)). For the oblique incidence case (averaged uniformly over the unit sphere) the lateral localization precision is σ_{xy} = 4.6 nm, azimuth and polar angle precision are $\sigma_\phi = 2.4°$, $\sigma_\theta = 1.6°$, and signal and background photon count precision are 49 photons and 0.35 photons per pixel (Fig. 6(b)).

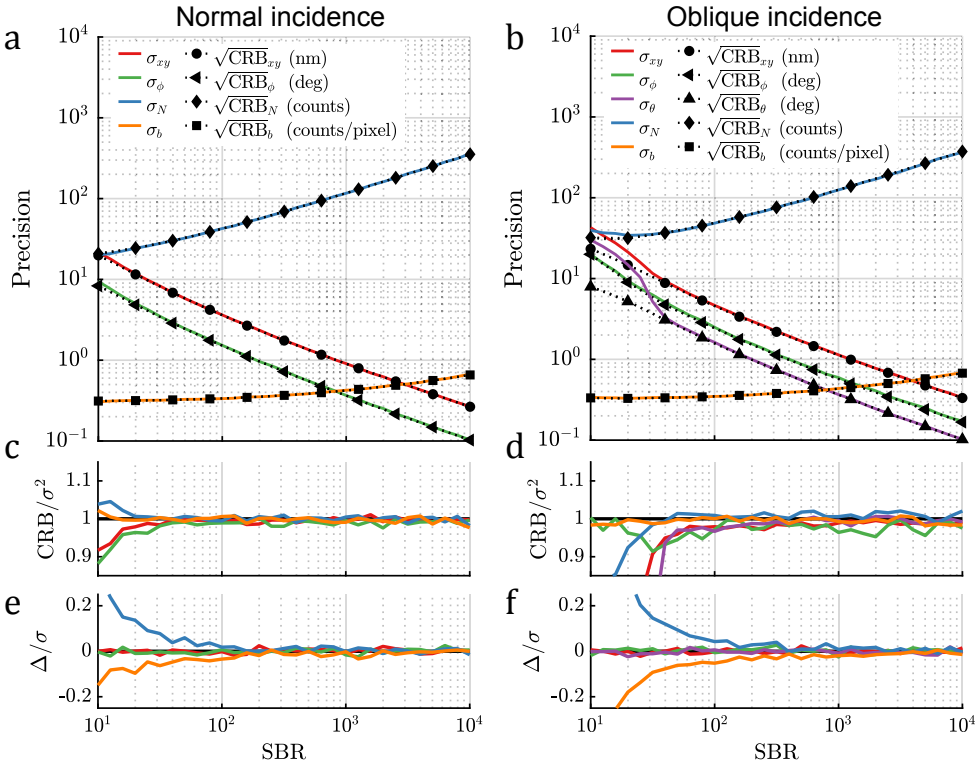

Fig. 6. Simulation study of signal-to-background ratio (SBR = $N/b, b$ = 10). (a) The precision for the estimated parameters (colored lines) as a function of the SBR compared to the CRB (black lines) for the in-plane and (b) oblique polarization mode. (c-d) The estimator efficiency (CRB/σ^2) for the in-plane polarization and oblique polarization mode. (e-f) The estimator bias (Δ/σ) for the in-plane polarization and oblique polarization mode.

Figure 6(c-d) show the estimator efficiency given by the ratio CRB/σ^2. Our estimator performs at the precision bound over a broad range of photon counts. At very low SBR values, however, this is no longer the case. We find that the estimator efficiencies drop below 95% for SBR<30 and SBR<50 for the normal incidence and oblique incidence modes, respectively.

Biomedical Optics EXPRESS

Figure 6(e-f) show the estimator bias Δ relative to the precision σ. A bias arises at low photon counts SBR$<10^2$ where the estimator tends to overestimate the signal photon count and underestimate the background photon count by a few percentage points of the precision. This mismatch is much smaller than the conventional Gaussian model, where up to 30% photon count underestimation commonly occurs [49,50]. We also observe that our MLE with a vectorial PSF model achieves the CRB at very high photon counts SBR$>10^3$, which is not the case for modulation enhanced SMLM when using a Gaussian model due to large photon count errors [33].

4.3. Estimation performance dependence on polarization quality

4.3.1. Normal incidence

Simulations were performed to obtain insight into the required accuracy for the illumination polarization parameters. Figure 7 shows the results of this analysis for the normal incidence case with a relatively low signal count SBR = 1000/10. A significant drawback of this excitation mode is that only the azimuthal angle is modulated. When the molecules are tilted away from the polarization plane, i.e. if θ is less than 90° the performance worsens due to model mismatch (Fig. 7(a,c)). This mismatch is apparent as the photon count bias accumulates up to $\pm 1\sigma$ if θ deviates from the nominal 90° by 18°. This appears to be the same deviation beyond which the efficiency of the estimator is compromised. Therefore attention must be taken if these tilted molecules are included in the estimation process as their contribution limits the overall localization precision.

The CRB performance as a function of the ellipticity angle τ, or equivalently the (amplitude) extinction ratio $\kappa = \cot \tau$, was shown in Fig. 3. There, the assumption was that the polarization parameters are correctly calibrated, which is not always the case in practice. Figure 7(b,d) shows the results when the estimator assumes perfect linearly polarized excitation, whereas the ground-truth extinction ratio is varied. It is seen that the assumption of perfect linear polarization is valid for ground-truth extinction ratios above ~20. When the ground-truth extinction ratio is too low, the estimator no longer reaches the lower bound as the imperfect polarization induces photon count biases. Intensity extinction ratios down to 12:1 have been reported in the literature for similar methods [30], and in these cases, it becomes essential to modify the estimator to take calibrated, non-perfect, excitation polarization states into account. These imperfect extinction ratios, in combination with considering molecules with out-of-plane tilt in the analysis, may be contributing factors why the reported precision in [30] falls short of the CRB derived in this paper.

4.3.2. Oblique incidence

In the oblique incidence mode the full orientation is estimated, and no deterioration of performance by dipoles tilted from the image plane occurs. On the downside now the angle of incidence β must be calibrated as well. Figure 8 shows the results of the sensitivity analysis for the oblique incidence case. The lower limit for the extinction ratio remains about the same, i.e. for values below approximately 20, an experimentally determined value must be used in the estimator (Fig. 8(a,c)). It is seen that orientation parameters are the first to drop in estimator efficiency when the extinction ratio is lowered.

The oblique incidence mode requires the calibration of the different directions of incidence of the polarized excitation beams. The estimator maintains an efficiency above 95% for errors $|\Delta\beta|<1°$ in the angle of incidence (Fig. 8(b)). If the angle β is inaccurately known then there will be biases in the estimated orientations that depend on the ground truth dipole orientation. The error in the polar angle θ is typically not worse than the error in β itself in the range $|\Delta\beta|<3°$, however, when averaged over all orientations this bias averages out to zero and instead contributes

Biomedical Optics EXPRESS

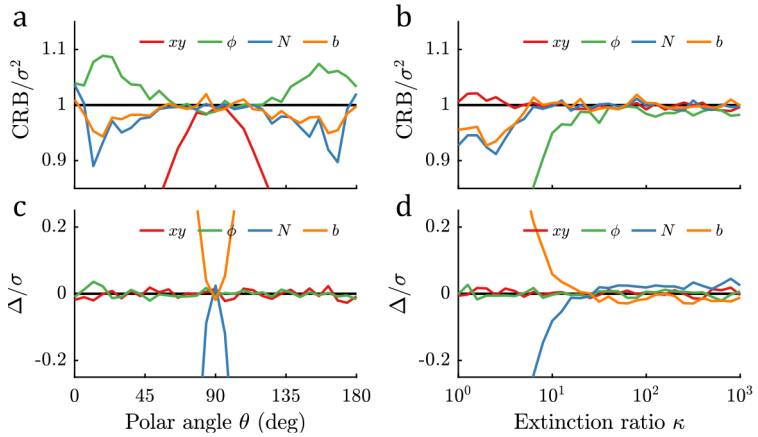

Fig. 7. Sensitivity analysis of in-plane polarization parameters (SBR = $N/b = 1000/10$). (a,c) The estimator efficiency (CRB/σ^2) and bias (Δ/σ) as a function of dipole polar angle. (b,d) The estimator efficiency and bias as a function of a ground-truth extinction ratio where the estimation assumes perfect linearly polarized excitation.

to the degradation of precision (Fig. 8(b,d)). To achieve minimal errors, the angle of incidence β should be calibrated to within at least 0.5°.

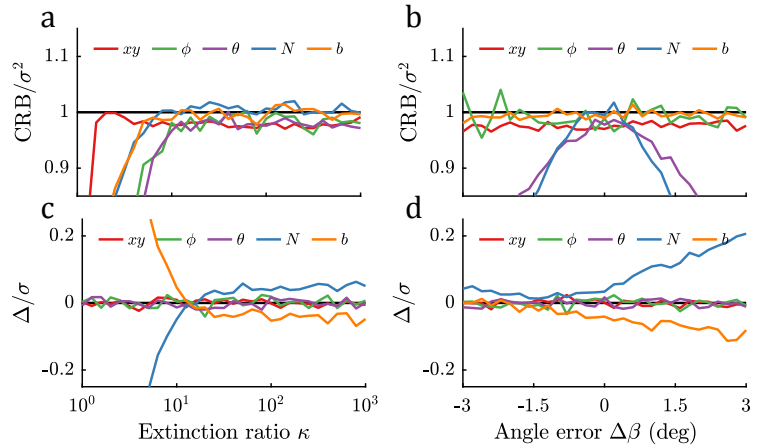

Fig. 8. Sensitivity analysis of polarization parameters (SBR = $N/b = 1000/10$). (a,c) The estimator efficiency (CRB/σ^2) and bias (Δ/σ) as a function of extinction ratio where the estimation assumes perfect linearly polarized excitation, (b,d) as a function of a constant angle error $\Delta\beta$ between the estimation and the ground-truth polarization steps.

5. Experimental setup

We have developed a microscope setup with accurate control of the excitation polarization in order to demonstrate the proposed high-precision orientation estimation principles. The key idea is to combine rotation of linear polarization with 2D galvo mirrors to quickly reposition the excitation beam to different positions in the back focal plane of the microscope, resulting in fast switching of the direction of incidence of the excitation beam. The desired level of control of

Biomedical Optics EXPRESS

the polarization state and direction of incidence requires an intricate alignment procedure and calibration steps described in detail in the following.

5.1. Optical layout

Fig. 9 shows the layout of our optical system with polarization control and consists of the following components. The polarization of the laser (FKL532.100.CWA.L, Omicron) is cleaned up by linear polarizer LP1 (GTH5-A, Thorlabs), the throughput of linearly polarized light is optimized with a $\lambda/4$ waveplate (AQWP05M-600, Thorlabs) and $\lambda/2$ waveplate (WPH05ME-532, Thorlabs). The Acousto-Optic Modulator (AOM) (TEM-85-2, Brimrose) modulates the amount of light coupled into a polarization maintaining fibre (P3-488PM-FC-2, Thorlabs) by lens L1 (C230TMD-A, Thorlabs). Lens L2 (N PLAN L 20x/0.35, Leica) collimates the light from the fibre output, by coupling through the polarization maintaining fibre the beam is spatially filtered and results in a Gaussian beam-profile. After the fibre the excitation laser spectrum is cleaned up by filter F1 (FF01-532/18, Semrock) and the polarization by LP2 (GTH5-A, Thorlabs). Hereafter the fast axis of the Pockels cell (EM508-2T-F-AR532, Leysop) is oriented 45 degrees to the vertical transmission axis of LP2 and the fast axis of the Babinet-Soleil compensator (SBC-VIS, Thorlabs) is perpendicular to the transmission axis of LP2. The plane in-between the 2D galvo mirrors (GVS002, Thorlabs) is relayed via the lenses L3 (AC254-080-A-ML, Thorlabs), L4 (AC254-300-A-ML, Thorlabs), L5 (AC254-150-A-ML, Thorlabs) and the objective lens (CFI Apo TIRF 100XC Oil, Nikon) to the sample plane. The sample is mounted through a collection of stages, (M-111.1DG with C-863, PI) for the rough z positioning, (P-517.3CL with E-710.4CL, PI) for the fine xyz translation and (H117N2IX, Prior) for rough xy translation. The dichroic mirror (Di03-R405/488/532/635-t1, Semrock) splits the excitation and emission path. After an elliptical mirror (BBE1-E02, Thorlabs) and emission filter F2 (FF01-582/64, Semrock) the emitted fluorescence is focused onto the camera (ORCA-Flash4.0 V2, Hamamatsu) by a tube lens (ITL200, Thorlabs). The exposure output of the camera triggers a data acquisition card (PXIe-6363, NI) to switch between illumination states and sends corresponding signals to the Pockels cell amplifier (M5000, Leysop), AOM RF driver (FFA-85-B1-F1, Brimrose) and the galvo mirrors.

5.2. Alignment

To achieve a high extinction ratio of linearly polarized light in the sample plane the polarization optics needs to be properly aligned. The polarization rotation is done with a Pockels cell, Babinet-Soleil compensator and a dichroic mirror. To rotate the polarization whilst maintaining a linear polarization it is necessary to have a $\lambda/4$ waveplate after the Pockels cell, with the fast axis aligned perpendicular to the transmission axis of LP2. The dichroic mirror can induce phase differences between s and p polarized light and thus a diagonally polarized incident beam will no longer be linearly polarized after reflection [51]. To compensate for this effect the Babinet-Soleil compensator can be aligned to either the s or p axis of the dichroic mirror to compensate for any induced phase differences. However, to avoid the use of another $\lambda/4$ waveplate, the Babinet-Soleil compensator is adjusted such that, combined with the dichroic mirror, it has a net $\lambda/4$ wave retardance, aligned perpendicular with respect to LP2. For initial alignment two temporary polarizers are placed after LP2, the first one is cross-polarized with LP2, the second is placed in between and aligned 45° to LP2 such that it maximizes the transmission. Thereafter the crossed polarizer is removed and the light entering the Babinet-Soleil compensator is polarized 45° with respect to LP2. The Babinet-Soleil compensator is then adjusted such that the light after the dichroic mirror is circularly polarized, which is achieved by minimizing the intensity variation (<1.5%) measured with a continuously rotating linear polarizer (LPVISC100-MP2, Thorlabs) in an automatic rotation mount (8MPR16-1, Standa) on a power meter (PM100D and S121C,

Biomedical Optics EXPRESS

Thorlabs). Thereafter the temporary polarizer is removed giving the polarization in the sample plane the desired linear polarization.

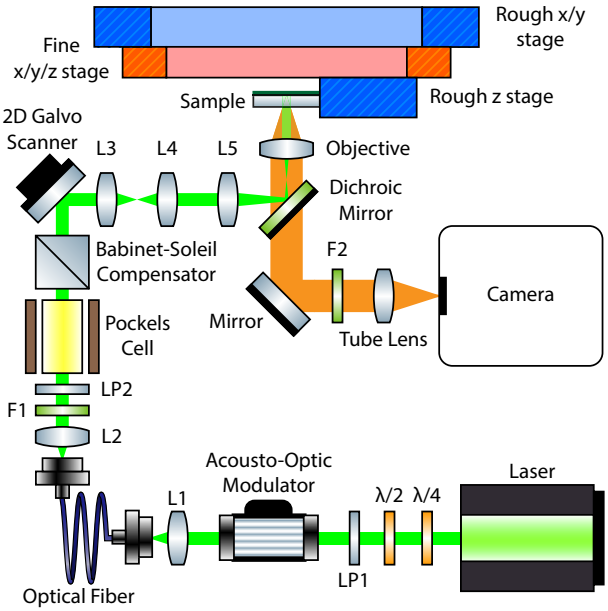

Fig. 9. Schematic of the optical layout of the widefield microscope with polarization control and beam angle steering in the excitation path.

The modulation of the excitation polarization is achieved with the Pockels cell. To get the best performance, the Pockels cell needs to be rotationally aligned. The tip and tilt can be optimized by placing the Pockels cell between crossed polarizers, then a Maltese cross pattern can be visualized by diffusing the beam with a lens tissue. The tip and tilt is adjusted such that the Maltese cross is centered on the main beam. The roll is adjusted with a voltage applied to the Pockels cell so that the transmission through crossed polarizers is maximized, making the fast axis at 45° to LP2. With the crossed polarizer removed the extinction ratio is measured with the rotating polarizer for varying Pockels cell voltages. The Babinet-Soleil compensator is slightly adjusted to get the purest linear polarization over the full Pockels cell range.

The galvo mirrors are a single unit containing two separate galvo mirrors, one for each axis and spaced 10 mm apart. This unit is positioned such that a reversely propagating beam from an alignment laser (CPS532, Thorlabs) pointed down from the objective in Fig. 9 is focused in between the two galvo mirrors. Due to the distance between these two mirrors the plane of tipping and tilting for the forward propagating beam does not coincide.

5.3. Calibration

The first calibration step is to relate the applied polarizations to the camera frame of reference. This is done in two steps, firstly connecting the positions in the back focal plane of the objective lens that are addressed with the galvo mirrors with respect to the camera plane. To that end we scan each individual galvo mirror in a defocused liquid ATTO 565 sample inducing a shift in the illumination pattern that is visible on the camera. Tracking this shift gives an angle of $0.005° \pm 0.005°$ for the x galvo mirror and an angle of $88.86° \pm 0.05°$ for the y galvo mirror, close to the desired 0° and 90° (compare Fig. 10(a)).

Secondly, the Pockels cell control voltage is calibrated to align the s and p-polarization orientations to the direction of incidence set by the galvo mirrors. Figure 10(b) shows the

Biomedical Optics EXPRESS

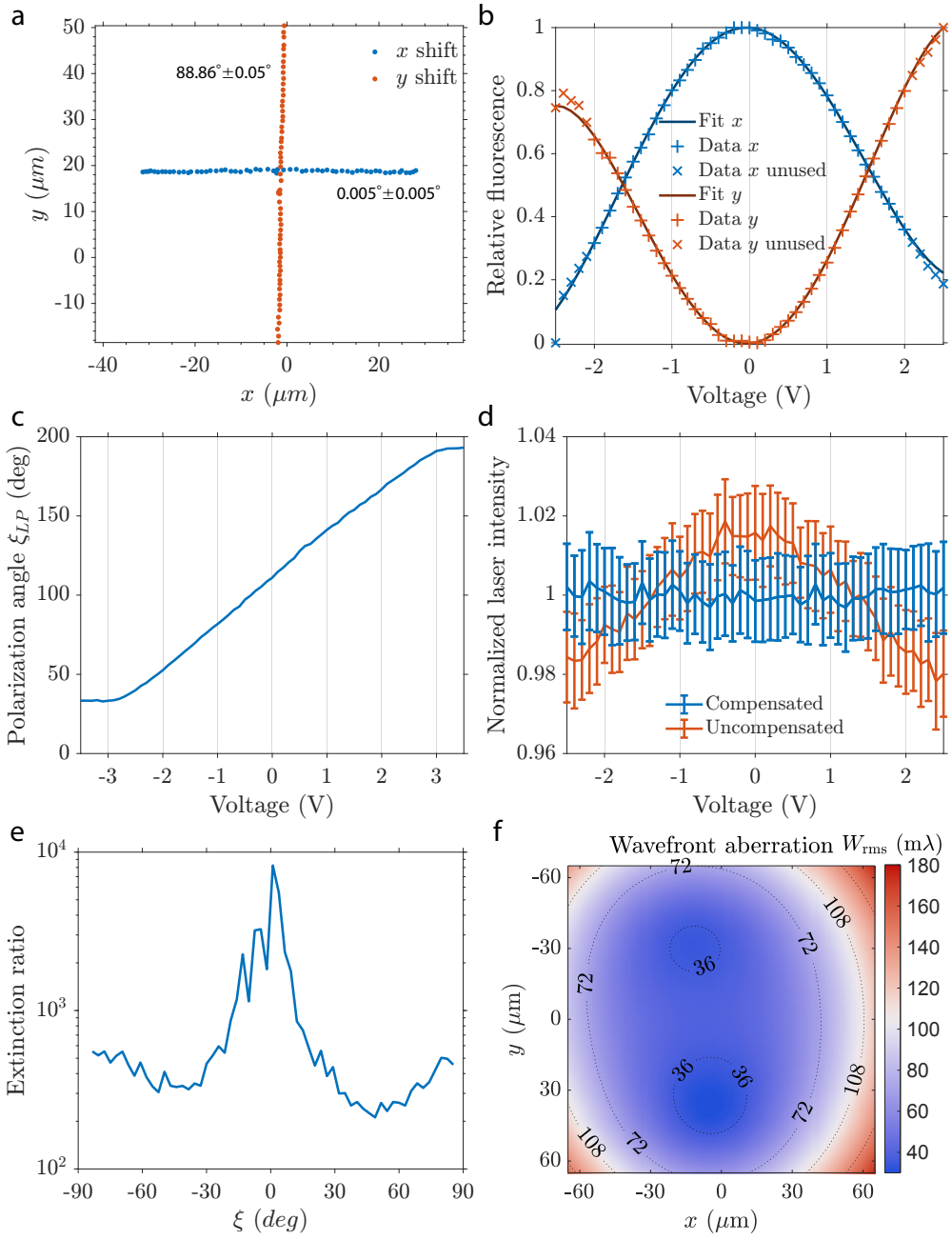

Fig. 10. Polarization and aberration calibration. (a) Illumination scan orientations for each respective galvo mirror axis. (b) Fluorescence modulation of beads with illumination just beyond the critical angle with varying polarization states. (c) Polarization angle as a function of the Pockels cell control voltage. (d) Intensity variation of s and p-polarized light in the sample plane, compensated by varying the incident power with the AOM. (e) Extinction ratio (intensity) for different polarization orientation angles. (f) Total measured wavefront aberration level in the imaged field for the microscope setup. The dotted contour lines show the aberration level in relation to Maréchal's diffraction limit (<72 mλ).

Biomedical Optics EXPRESS

modulation of fluorescence of beads on the cover slip for x and y galvo settings that result in directions of incidence a few degrees beyond the critical angle. A maximum is obtained for a Pockels cell control voltage of −0.0351 V for the x galvo, implying that at this voltage the polarization is p-polarized [52]. Similarly for the y galvo axis there is a minimum at a Pockels cell control voltage of −0.0350 V implying the light is s-polarized. This gives voltage references that calibrate the excitation polarizations to the directions of incidence, which are itself calibrated to the camera xy coordinate frame. In this way the applied polarization states are known in the camera xy coordinate frame, with the advantage that this does not require challenging manual co-alignment of optical components [30], but instead derives fully from fluorescence data.

In a next calibration step to determine the rotation response of the Pockels cell, the change of the polarization angle ξ_{LP} is measured as a function of the Pockels cell control voltage. This is done using a rotating linear polarizer and rotation mount (mentioned in section 5.2), combined with a photodiode (DET100A/M, Thorlabs), the angle ξ_{LP} is defined with respect to the zero point of the rotation mount. Figure 10(c) shows that there is a rotation of $28.53\,^\circ/V$ and that the response is linear between ±2 V. By combining this angle-voltage response with the previous s and p polarization calibration it is now possible to determine ξ, the polarization orientation angle with respect to the camera coordinate frame, as a function of the Pockels cell control voltage.

A final polarization calibration step involves equalization of amplitude differences between the s and p-polarized components, that can arise from differences in reflectivity of the dichroic mirror with polarization. This effect can be compensated by adjusting the AOM that controls the laser power. Figure 10(d) shows 3% variation in laser power as the polarization is rotated with the Pockels cell, compensating with the AOM the variation can be reduced to 0.16% (standard deviation of the mean value). Lastly, the intensity extinction ratio is measured using the rotating linear polarizer, lock-in amplifier (SR830, SRS) and optical chopper (MC2000-EC, Thorlabs), and is found to be larger than 211:1 for all polarization orientation angles ξ and 851:1 on average (Fig. 10(e)). The extinction ratio still peaks at $\xi = 0°$ and $\xi = \pm 90°$ as the light incident on the dichroic mirror is pure s or p-polarized and deteriorates slightly towards $\xi = \pm 45°$.

In the MLE fitting procedure we have used experimentally obtained optical aberration values [53] as a function of the position in the imaged Field Of View (FOV), generated from a calibration measurement on a sparse bead sample. This aberration calibration procedure [16] guarantees knowledge of the optical aberrations with an accuracy well below <36 mλ [50], which is needed to minimize non-uniform biases in the localization and orientation estimation. Figure 10(f) shows the measured aberration levels across the FOV indicating sizeable aberrations throughout, even beyond the diffraction limit at the edges of the FOV.

6. Experimental results

6.1. Polarization modulation fitting

As a proof of principle, we imaged single fluorophores (ATTO 565) embedded in polymethyl methacrylate (PMMA). These single emitters are rotationally constrained in the PMMA resin (details on the sample preparation are presented in Supplement 1 section 2). The sample was sequentially illuminated with 3 polarization states each shifted by $\Delta\xi = 60°$ at normal incidence. Every individual frame had an exposure time of 300 ms and a laser intensity of 100 W/cm^2. We estimated the position and in-plane orientation of several isolated single molecules from the sequence of images with different polarization states (Fig. 11). There is a good agreement between the data on the left and the fit on the right (mean $\chi^2 = 1.7$). For relatively high photon counts the shape change of the PSF can be observed. An elongation of the PSF shape can be seen (diagonally to the bottom left for the first molecule and vertically for the second molecule). The PSF shape is not clearly perceivable at lower photon counts but still needs to be taken into account to make the best possible estimate of position and orientation.

Biomedical Optics EXPRESS

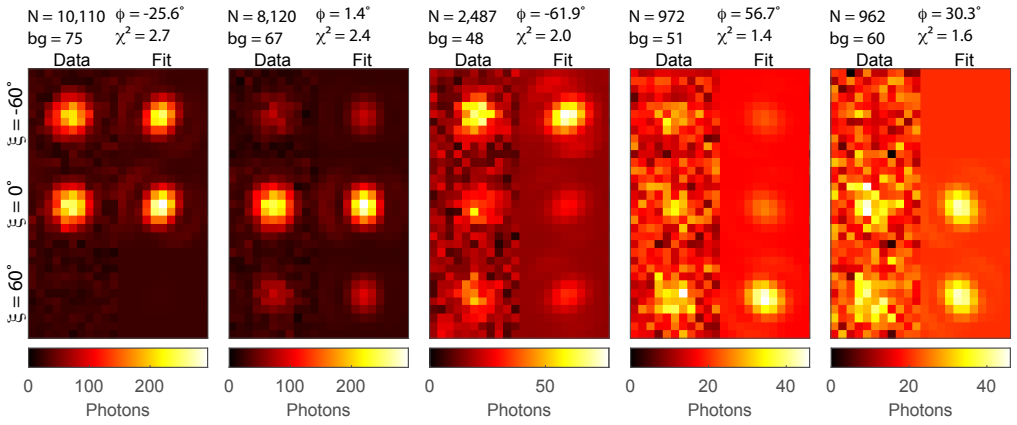

Fig. 11. Experimental polarization modulation of individual fluorophores and corresponding fit. Each row is illuminated with a different in-plane polarization (ξ). Each column shows a single fluorophore with the data on the left and fit on the right. The estimated parameters (N, b and ϕ) per set of frames are displayed at the top, along with the quality of fit (χ^2).

6.2. *Experimental precision with normal incidence*

Next, we continued imaging ATTO 565 molecules embedded in PMMA. In this case 50 cycles of 3 polarization states are acquired at various laser powers and camera exposure times (see Supplement 1 section 3 for additional details). This expands the distribution of photon counts such that the angular estimation precision can be analyzed over a wide range of photon counts. To analyze the experimental precision multiple localizations of the same single-molecules are linked (Supplement 1 (section 3)) and analyzed if they are on for more than 4 cycles. On average we obtained 8.3 estimates for each molecule from which we calculated the orientation estimation precision as the standard deviation of the orientation estimates (Fig. 12(a)). The average precision σ_ϕ and $\sqrt{\mathrm{CRB}_\phi}$ are obtained from least squares fits of a line with slope proportional to $1/\sqrt{N}$. The information content of the photons on the camera is efficiently used as is evident from the fit between the experimental precision and the CRB, with the experimental precision only 16% above the CRB on average. This experimental azimuthal precision is a factor of about 2.3 better than the previously achieved experimental precision [30]. We furthermore confirm the theoretical prediction that there is a slight variation in precision with the molecular orientation in relation to the three excitation polarization directions (Fig. 12(b)).

We attempted the estimation of both the in-plane and out-of-plane angle of the molecules according to the oblique incidence method. Unfortunately, this did not result in reliable fit outcomes, as we found a bias in the polar angle towards the in-plane orientation. One experimental difficulty we encountered relates to a shift of the Gaussian excitation profile across the FOV upon changing the direction of incidence of the illumination beam with the 2D galvo system. This resulted in undesired intensity variations for each molecule that are not coupled to the polarization modulation. This could be compensated for with an additional calibration step, as e.g. in Ref. [54], but did not turn out to work completely satisfactorily. The use of a single 2D scanning mirror (e.g. a piezo or MEMS mirror) could potentially solve this problem. The impact of non-zero polarization ellipticity and of dipole wobbling could also be assessed in a future study.

Biomedical Optics EXPRESS

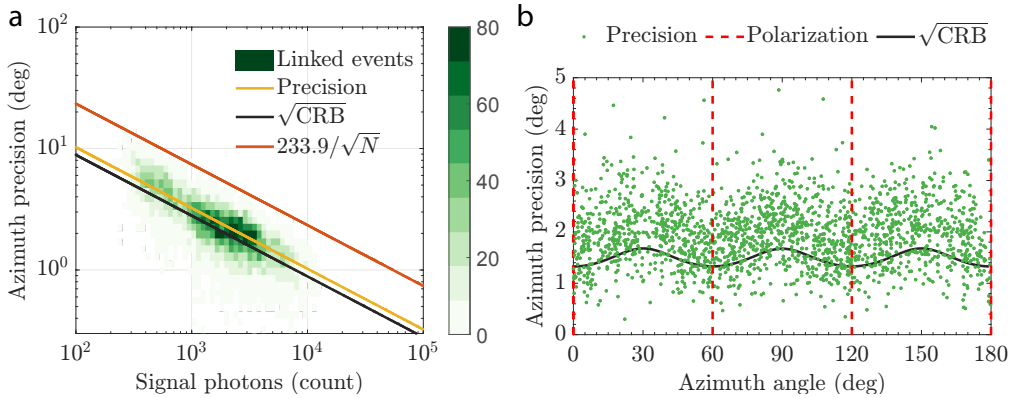

Fig. 12. Assessment of experimental precision. (a) Azimuthal precision from linked localizations ($t_{on} \geq 15$) compared to the estimated photon count (green histogram indicating the number of measurements). The average experimental precision (yellow), theoretical $\sqrt{\text{CRB}}$ (black), and current state-of-the-art [30] precision (red) are also indicated. The photon count range is expanded by combining 8 experiments with varying laser intensities and camera exposure. (b) Azimuthal precision compared to the azimuthal angle for photon counts one standard deviation around the average. The applied polarizations are indicated (dashed red), as well as the $\sqrt{\text{CRB}}$ (black), which is calculated from the median photon count ($\tilde{N} = 2696$) and background ($\tilde{b} = 68$).

7. Discussion

7.1. Imaging speed

In-plane modulation is well suited for determining the in-plane orientation of molecules in typical SMLM experiments as the modulation of the illumination polarization state can be very fast. The AOM and Pockels cell can be switched easily within the readout time of the camera, which makes the camera speed the limiting factor. It is possible to acquire at least 6 frames during the on-time of fluorophores [33]. For oblique illumination, re-positioning the galvo mirrors (~ 3 ms) only becomes a limiting factor when using high framerate readout over small regions of interest on the camera (less than 600x600 pixels), as the readout time scales with the amount of lines that are read out for an sCMOS camera. As the orientation estimation is photon efficient it is feasible to reduce the exposure time down to ~ 10 ms.

7.2. Rotational diffusion

The main limitation of the current image formation model is the assumption that the emitter is stationary (section 2), i.e., that it has a completely fixed pose in space with negligible rotational diffusion. This assumption could be correct in applications where the rotational mobility of the molecule can be regarded as completely restricted at typical frame rates of milliseconds [10]. The label molecules in a biological sample, however, undergo rotational diffusion and wobble around an average orientation [55]. For instance, common intercalators (e.g., SYTOX orange) used in λ-DNA experiments report rotational diffusion within a cone with a semi-cone angle on the order of $20° - 30°$ [16,30,56]. When not taken into account, this inadvertently affects the estimated photon counts and thereby worsens the quality of the orientation estimation. An interesting extension to the present work is therefore to parameterize the rotational diffusion and jointly estimate these parameters together with the molecule's position and preferential orientation. As our method takes both the intensity modulation and PSF shape into account simultaneously it should be easier to disentangle background fluorescence and degrees of wobbling. For this a PSF

Biomedical Optics EXPRESS

model that is a weighted sum of the fully free and fully fixed dipole PSFs, which is appropriate for fast rotational diffusion, seems the best starting point [16,57]. Smart probing with more variations in excitation states could also be used to identify asymmetrical rotational diffusion.

7.3. Additional parameters

The CRB performance with respect to the orientation estimation or any other parameters could be improved by combining PSFs engineered towards the specific problems at hand with modulation of the excitation polarization. For example, such PSF designs could be designed to estimate axial position information, which would enable the generalization to the case of 3D SMLM. This could, however, come at the cost of reduced lateral localization precision and a limited axial working range because axial localization usually entails a decrease of the signal-to-background ratio. An interesting question to investigate regarding the combination of PSF engineering and polarization modulation would be the quantification of possible differences between the absorption and emission dipole moment [37,58].

7.4. Multiphoton excitation

Multiphoton excitation induces a nonlinear dependence of the fluorescence excitation efficiency on dipole orientation that can be used to enhance the estimation precision. For example, for two-photon excitation, the intensity of fluorescence is proportional to the fourth power of the excitation amplitude $\left|\hat{\mathbf{d}} \cdot \hat{\boldsymbol{\epsilon}}\right|^4$ [59]. This fourth power dependence improves the polarization contrast, and therefore the CRB precision can, in principle, be reduced. For example, in the case of normal incidence described in section 3, the modulation function now takes the following form assuming that $\tau = 0$:

$$P_m(\phi) = \frac{8}{3M} \cos^4(\phi - \xi_m). \tag{25}$$

The Fisher-information element can be determined by substituting Eq. (25) in the second term of Eq. (9):

$$F_{\phi\phi} = \frac{16N}{3M} \sum_{m=1}^{M} [1 - \cos(4\phi - 4\xi_m)] = \frac{16N}{3} \tag{26}$$

which yields the precision limit:

$$\sigma_\phi = \frac{\sqrt{3}}{4\sqrt{N}}. \tag{27}$$

It is seen that the uncertainty is smaller by a factor of $\sqrt{3}/2 \approx 0.87$ as compared to the precision in section 3.

7.5. Oblique illumination at the critical angle

A particularly interesting case for polarization modulation at oblique incidence is the case of illumination exactly at the critical angle. In that case the wavevector in the sample medium $\mathbf{k_t}$ is fully in the sample (xy) plane, and as a consequence the p-polarization vector is then along the optical (z) axis, where as the s-polarization vector is in the sample plane orthogonal to $\mathbf{k_t}$. Furthermore, the phase shifts for the p and s-polarized components are both zero, as opposed to the case of an angle of incidence beyond the critical angle [52,60]. This would instead induce an elliptical polarization in the sample when rotating to an incident linear polarization intermediate to the p and s-polarization. This can be avoided at the critical angle, enabling continuous rotation of linearly polarized light with an arbitrary orientation. A difference between the amplitude of transmission for the p and s-polarization components does remain, which would introduce a rotation of the linear polarization inside the sample relative to the incidence polarization, which would have to be taken into account. In order to avoid the TIRF induced polarization phase

Biomedical Optics EXPRESS

differences and achieve an amplitude extinction ratio $\kappa \geq 20$, the incident angle needs to be within a challenging 0.06° of the critical angle.

8. Conclusion

In conclusion, we proposed a concept to estimate molecular orientation that is compatible with localization microscopy by using polarized excitation. The theoretical performance limits were quantified using a Cramér-Rao bound analysis in terms of the excitation polarization parameters. To this end, analytic expressions for the CRB for cases of normal and oblique incidence were derived. Numerical simulations were performed to evaluate the performance of the polarization modulation method as a function of SBR and to assess the required accuracy of the excitation polarization states in experiments. We showed that a precision below 2.5° can be achieved in principle for both the azimuthal and polar angle with only 1000 photons in the presence of 10 background photons per pixel. The attained estimator precision is better than existing polarization modulation methods due to both the MLE based procedure and the inclusion of the PSF shape rather than just analyzing intensity modulations. The method is considered beneficial for orientation measurements where standard SMLM resolution is desired, particularly for cases where only dim fluorophores are available. We have built a microscope setup for testing the proposed polarization modulation methods, detailing the necessary calibration protocols. The setup enables polarization modulation with a linear polarization purity characterized with an average (intensity) extinction ratio of 851:1. In a proof-of-principle experiment on single molecules embedded in PMMA we achieved an experimental in-plane orientation precision only 16% above the CRB, and a factor 2.3 better than previously reported results [30]. In future work we strive for an experimental demonstration of the in-plane and out-of-plane orientation precision for the oblique illumination scheme. Other future steps worth investigating are the incorporation of a rotational diffusion model, and the combination of polarization modulation with recent PSF engineering methods, reaping the benefits of both approaches to make yet another step in precision.

Funding. National Institutes of Health (U01EB021238); European Research Council (648580).

Disclosures. The authors declare no conflicts of interest.

Data availability. Data underlying the results presented in this paper are not publicly available at this time but may be obtained from the authors upon reasonable request.

Supplemental document. See Supplement 1 for supporting content.

References

1. S. T. Hess, T. P. Girirajan, and M. D. Mason, "Ultra-high resolution imaging by fluorescence photoactivation localization microscopy," Biophys. J. **91**(11), 4258–4272 (2006).
2. E. Betzig, G. H. Patterson, R. Sougrat, O. W. Lindwasser, S. Olenych, J. S. Bonifacino, M. W. Davidson, J. Lippincott-Schwartz, and H. F. Hess, "Imaging intracellular fluorescent proteins at nanometer resolution," Science **313**(5793), 1642–1645 (2006).
3. M. J. Rust, M. Bates, and X. Zhuang, "Sub-diffraction-limit imaging by stochastic optical reconstruction microscopy (STORM)," Nat. Methods **3**(10), 793–796 (2006).
4. A. Sharonov and R. M. Hochstrasser, "Wide-field subdiffraction imaging by accumulated binding of diffusing probes," Proc. Natl. Acad. Sci. U. S. A. **103**(50), 18911–18916 (2006).
5. B. Huang, W. Wang, M. Bates, and X. Zhuang, "Three-dimensional super-resolution imaging by stochastic optical reconstruction microscopy," Science **319**(5864), 810–813 (2008).
6. M. P. Backlund, M. D. Lew, A. S. Backer, S. J. Sahl, and W. E. Moerner, "The role of molecular dipole orientation in single-molecule fluorescence microscopy and implications for super-resolution imaging," ChemPhysChem **15**(4), 587–599 (2014).
7. E. J. Peterman, H. Sosa, L. S. Goldstein, and W. E. Moerner, "Polarized fluorescence microscopy of individual and many kinesin motors bound to axonemal microtubules," Biophys. J. **81**(5), 2851–2863 (2001).
8. E. Toprak, J. Enderlein, S. Syed, S. A. McKinney, R. G. Petschek, T. Ha, Y. E. Goldman, and P. R. Selvin, "Defocused orientation and position imaging (DOPI) of myosin V," Proc. Natl. Acad. Sci. U. S. A. **103**(17), 6495–6499 (2006).
9. H. A. Shaban, C. A. Valades-Cruz, J. Savatier, and S. Brasselet, "Polarized super-resolution structural imaging inside amyloid fibrils using Thioflavine T," Sci. Rep. **7**(1), 12482 (2017).

Biomedical Optics EXPRESS

10. M. Wang, J. M. Marr, M. Davanco, J. W. Gilman, and J. A. Liddle, "Nanoscale deformation in polymers revealed by single-molecule super-resolution localization-orientation microscopy," Mater. Horiz. **6**(4), 817–825 (2019).
11. J. Lu, H. Mazidi, T. Ding, O. Zhang, and M. D. Lew, "Single-molecule 3D orientation imaging reveals nanoscale compositional heterogeneity in lipid membranes," Angew. Chem. **132**(40), 17725–17732 (2020).
12. J. Engelhardt, J. Keller, P. Hoyer, M. Reuss, T. Staudt, and S. W. Hell, "Molecular orientation affects localization accuracy in superresolution far-field fluorescence microscopy," Nano Lett. **11**(1), 209–213 (2011).
13. M. D. Lew, M. P. Backlund, and W. E. Moerner, "Rotational mobility of single molecules affects localization accuracy in super-resolution fluorescence microscopy," Nano Lett. **13**(9), 3967–3972 (2013).
14. M. P. Backlund, M. D. Lew, A. S. Backer, S. J. Sahl, G. Grover, A. Agrawal, R. Piestun, and W. E. Moerner, "Simultaneous, accurate measurement of the 3D position and orientation of single molecules," Proc. Natl. Acad. Sci. **109**(47), 19087–19092 (2012).
15. A. S. Backer, M. P. Backlund, M. D. Lew, and W. E. Moerner, "Single-molecule orientation measurements with a quadrated pupil," Opt. Lett. **38**(9), 1521 (2013).
16. C. N. Hulleman, R. Ø. Thorsen, E. Kim, C. Dekker, S. Stallinga, and B. Rieger, "Simultaneous orientation and 3D localization microscopy with a Vortex point spread function," Nat. Commun. **12**(1), 5934 (2021).
17. T. J. Gould, M. S. Gunewardene, M. V. Gudheti, V. V. Verkhusha, S. R. Yin, J. A. Gosse, and S. T. Hess, "Nanoscale imaging of molecular positions and anisotropies," Nat. Methods **5**(12), 1027–1030 (2008).
18. S. R. P. Pavani, J. G. DeLuca, and R. Piestun, "Polarization sensitive, three-dimensional, single-molecule imaging of cells with a double-helix system," Opt. Express **17**(22), 19644 (2009).
19. S. Stallinga and B. Rieger, "Position and orientation estimation of fixed dipole emitters using an effective Hermite point spread function model," Opt. Express **20**(6), 5896 (2012).
20. C. A. V. Cruz, H. A. Shaban, A. Kress, N. Bertaux, S. Monneret, M. Mavrakis, J. Savatier, and S. Brasselet, "Quantitative nanoscale imaging of orientational order in biological filaments by polarized superresolution microscopy," Proc. Natl. Acad. Sci. U. S. A. **113**, E820–E828 (2016).
21. C. V. Rimoli, C. A. Valades-Cruz, V. Curcio, M. Mavrakis, and S. Brasselet, "4polar-STORM polarized super-resolution imaging of actin filament organization in cells," Nat. Commun. **13**(1), 301 (2022).
22. A. S. Backer, M. P. Backlund, A. R. Von Diezmann, S. J. Sahl, and W. E. Moerner, "A bisected pupil for studying single-molecule orientational dynamics and its application to three-dimensional super-resolution microscopy," Appl. Phys. Lett. **104**(19), 193701 (2014).
23. O. Zhang, J. Lu, T. Ding, and M. D. Lew, "Imaging the three-dimensional orientation and rotational mobility of fluorescent emitters using the Tri-spot point spread function," Appl. Phys. Lett. **113**(3), 031103 (2018).
24. V. Curcio, L. A. Alemán-Casta neda, T. G. Brown, S. Brasselet, and M. A. Alonso, "Birefringent Fourier filtering for single molecule coordinate and height super-resolution imaging with dithering and orientation," Nat. Commun. **11**(1), 5307 (2020).
25. O. Zhang, W. Zhou, J. Lu, T. Wu, and M. D. Lew, "Resolving the three-dimensional rotational and translational dynamics of single molecules using radially and azimuthally polarized fluorescence," Nano Lett. **22**(3), 1024–1031 (2022).
26. T. Chandler, S. Mehta, H. Shroff, R. Oldenbourg, and P. J. La Rivière, "Single-fluorophore orientation determination with multiview polarized illumination: modeling and microscope design," Opt. Express **25**(25), 31309 (2017).
27. A. T. Blanchard, J. M. Brockman, K. Salaita, and A. L. Mattheyses, "Variable incidence angle linear dichroism (VALiD): a technique for unique 3D orientation measurement of fluorescent ensembles," Opt. Express **28**(7), 10039 (2020).
28. M. Prummer, B. Sick, B. Hecht, and U. P. Wild, "Three-dimensional optical polarization tomography of single molecules," J. Chem. Phys. **118**(21), 9824–9829 (2003).
29. J. N. Forkey, M. E. Quinlan, M. A. Shaw, J. E. Corrie, and Y. E. Goldman, "Three-dimensional structural dynamics of myosin V by single-molecule fluorescence polarization," Nature **422**(6930), 399–404 (2003).
30. A. S. Backer, M. Y. Lee, and W. E. Moerner, "Enhanced DNA imaging using super-resolution microscopy and simultaneous single-molecule orientation measurements," Optica **3**(6), 659 (2016).
31. R. Henriques, M. Lelek, E. F. Fornasiero, F. Valtorta, C. Zimmer, and M. M. Mhlanga, "QuickPALM: 3D real-time photoactivation nanoscopy image processing in ImageJ," Nat. Methods **7**(5), 339–340 (2010).
32. F. Balzarotti, Y. Eilers, K. C. Gwosch, A. H. Gynnå, V. Westphal, F. D. Stefani, J. Elf, and S. W. Hell, "Nanometer resolution imaging and tracking of fluorescent molecules with minimal photon fluxes," Science **355**(6325), 606–612 (2017).
33. J. Cnossen, T. Hinsdale, R. Ø. Thorsen, M. Siemons, F. Schueder, R. Jungmann, C. S. Smith, B. Rieger, and S. Stallinga, "Localization microscopy at doubled precision with patterned illumination," Nat. Methods **17**(1), 59–63 (2020).
34. L. Gu, Y. Li, S. Zhang, Y. Xue, W. Li, D. Li, T. Xu, and W. Ji, "Molecular resolution imaging by repetitive optical selective exposure," Nat. Methods **16**(11), 1114–1118 (2019).
35. P. Jouchet, C. Cabriel, N. Bourg, M. Bardou, C. Poüs, E. Fort, and S. Lévêque-Fort, "Nanometric axial localization of single fluorescent molecules with modulated excitation," Nat. Photonics **15**(4), 297–304 (2021).
36. D. Axelrod, "Cell-substrate contacts illuminated by total internal reflection fluorescence," J. Cell Biol. **89**(1), 141–145 (1981).

Biomedical Optics EXPRESS

37. N. Karedla, S. C. Stein, D. Hähnel, I. Gregor, A. Chizhik, and J. Enderlein, "Simultaneous measurement of the three-dimensional orientation of excitation and emission dipoles," Phys. Rev. Lett. **115**(17), 173002 (2015).
38. B. R. Lentz, "Use of fluorescent probes to monitor molecular order and motions within liposome bilayers," Chem. Phys. Lipids **64**(1-3), 99–116 (1993).
39. M. Born, E. Wolf, A. B. Bhatia, P. C. Clemmow, D. Gabor, A. R. Stokes, A. M. Taylor, P. A. Wayman, and W. L. Wilcock, *Principles of Optics* (Cambridge University Press, 1999).
40. K. I. Mortensen, L. S. Churchman, J. A. Spudich, and H. Flyvbjerg, "Optimized localization analysis for single-molecule tracking and super-resolution microscopy," Nat. Methods **7**(5), 377–381 (2010).
41. S. Stallinga and B. Rieger, "Accuracy of the Gaussian point spread function model in 2D localization microscopy," Opt. Express **18**(24), 24461 (2010).
42. C. Smith, M. Huisman, M. Siemons, D. Grünwald, and S. Stallinga, "Simultaneous measurement of emission color and 3D position of single molecules," Opt. Express **24**(5), 4996 (2016).
43. J. Chao, E. Sally Ward, and R. J. Ober, "Fisher information theory for parameter estimation in single molecule microscopy: tutorial," J. Opt. Soc. Am. A **33**(7), B36 (2016).
44. B. Rieger and S. Stallinga, "The lateral and axial localization uncertainty in super-resolution light microscopy," ChemPhysChem **15**(4), 664–670 (2014).
45. M. R. Foreman and P. Török, "Fundamental limits in single-molecule orientation measurements," New J. Phys. **13**(9), 093013 (2011).
46. T. Ding, T. Wu, H. Mazidi, O. Zhang, and M. D. Lew, "Single-molecule orientation localization microscopy for resolving structural heterogeneities between amyloid fibrils," Optica **7**(6), 602 (2020).
47. O. Zhang and M. D. Lew, "Quantum limits for precisely estimating the orientation and wobble of dipole emitters," Phys. Rev. Res. **2**(3), 033114 (2020).
48. T. Ding and M. D. Lew, "Single-molecule localization microscopy of 3D orientation and anisotropic wobble using a polarized vortex point spread function," J. Phys. Chem. B **125**(46), 12718–12729 (2021).
49. C. Franke, M. Sauer, and S. V. De Linde, "Photometry unlocks 3D information from 2D localization microscopy data," Nat. Methods **14**(1), 41–44 (2016).
50. R. Ø. Thorsen, C. N. Hulleman, M. Hammer, D. Grünwald, S. Stallinga, and B. Rieger, "Impact of optical aberrations on axial position determination by photometry," Nat. Methods **15**(12), 989–990 (2018).
51. C. N. Hulleman, M. Huisman, R. J. Moerland, D. Grünwald, S. Stallinga, and B. Rieger, "Fluorescence polarization control for on-off switching of single molecules at cryogenic temperatures," Small Methods **2**(9), 1700323 (2018).
52. D. Axelrod, T. P. Burghardt, and N. L. Thompson, "Total internal reflection fluorescence," Annu. Rev. Biophys. Bioeng. **13**(1), 247–268 (1984).
53. M. Siemons, C. N. Hulleman, R. Ø. Thorsen, C. S. Smith, and S. Stallinga, "High precision wavefront control in point spread function engineering for single emitter localization," Opt. Express **26**(7), 8397 (2018).
54. K. Zhanghao, X. Chen, W. Liu, M. Li, Y. Liu, Y. Wang, S. Luo, X. Wang, C. Shan, H. Xie, J. Gao, X. Chen, D. Jin, X. Li, Y. Zhang, Q. Dai, and P. Xi, "Super-resolution imaging of fluorescent dipoles via polarized structured illumination microscopy," Nat. Commun. **10**(1), 4694 (2019).
55. I. Munro, I. Pecht, and L. Stryer, "Subnanosecond motions of tryptophan residues in proteins," Proc. Natl. Acad. Sci. U. S. A. **76**(1), 56–60 (1979).
56. A. S. Backer, A. S. Biebricher, G. A. King, G. J. Wuite, I. Heller, and E. J. Peterman, "Single-molecule polarization microscopy of DNA intercalators sheds light on the structure of S-DNA," Sci. Adv. **5**(3), eaav1083 (2019).
57. S. Stallinga, "Single emitter localization analysis in the presence of background," in *Optical Systems Design 2015: Computational Optics*, vol. 9630 D. G. Smith, F. Wyrowski, and A. Erdmann, eds. (SPIE, 2015), p. 96300V.
58. T. Ha, T. A. Laurence, D. S. Chemla, and S. Weiss, "Polarization spectroscopy of single fluorescent molecules," J. Phys. Chem. B **103**(33), 6839–6850 (1999).
59. W. L. Peticolas, J. P. Goldsborough, and K. E. Rieckhoff, "Double photon excitation in organic crystals," Phys. Rev. Lett. **10**(2), 43–45 (1963).
60. M. L. Martin-Fernandez, C. J. Tynan, and S. E. Webb, "A 'pocket guide' to total internal reflection fluorescence," J. Microsc. **252**(1), 16–22 (2013).